Journal of The Electrochemical Society, **158** (11) B1292-B1299 (2011)
0013-4651/2011/158(11)/B1292/8/$28.00 © The Electrochemical Society

Effect of Spatially-Varying GDL Properties and Land Compression on Water Distribution in PEM Fuel Cells

Yun Wang[a,*,z] **and Ken S. Chen**[b,*]

[a]*Renewable Energy Resources Lab and National Fuel Cell Research Center, Department of Mechanical and Aerospace Engineering, The University of California, Irvine, Irvine, California 92697-3975, USA*
[b]*Sandia National Laboratories, Livermore, California 94550, USA*

A multi-dimensional two-phase model of polymer electrolyte fuel cells is developed and employed to investigate through-plane water profiles with spatially-varying properties of gas diffusion layers (GDL) being accounted for. Both one-dimensional (1-D) and 2-D model predictions of liquid water profiles are presented. We find that the GDL properties can significantly affect the liquid through-plane profiles and local features, for example, liquid water may be trapped due to the spatial variation in GDL properties. Furthermore, land compression can cause GDL property variation in the in-plane direction, altering liquid water distribution. Model predictions are compared with experimental data from both neutron radiography and X-ray imaging. Reasonably good agreements are obtained.
 [DOI: 10.1149/2.015111jes]

Manuscript submitted May 2, 2011; revised manuscript received July 27, 2011. Published October 5, 2011.

Due to the growing environmental concerns and fossil fuel reserves being depleted rapidly, fuel cell technology has attracted a great deal of attention as one of the most promising clean energy converters. Among the different types of fuel cells, polymer electrolyte fuel cells (PEFCs), also called PEM (polymer electrolyte membrane or proton exchange membrane) fuel cells, are widely regarded as a viable candidate for automobile/portable applications, because of their high-energy density at low operating temperatures, quick start-up, high efficiency and zero CO_2 emissions. Water management is a central issue in PEM fuel cell development. On the one hand, water is essential to maintaining membrane ionic conductivity: high water content results in high membrane ionic conductivity, thus reducing the ohmic voltage loss. On the other hand, excess water leads to condensation and the ensuing fuel cell flooding, which reduces cell performance and further causes material degradation.[1–3] Liquid emerges when the vapor partial pressure reaches the saturation value. Liquid water must be efficiently removed from the reaction sites in the cathode catalyst layer (CL) where the oxygen reduction reaction (ORR) occurs, through the gas diffusion layer (GDL), and eventually out of the flow channels of a PEFC. Fig. 1 shows the schematic of a PEM fuel cell.

Reviews of PEM fuel cell modeling efforts have been conducted by several groups.[1–7] Notable early studies on two-phase flow modeling include Wang et al.,[8] He et al.,[9] Natarajan and Nguyen,[10] and You and Liu.[11] These models take into account several major two-phase transport mechanisms such as the capillary action and two-phase interaction. Based on these earlier work, isothermal two-phase phenomena have been investigated by several researchers subsequently.[12–17] Due to its inherently strong interaction with two-phase flow, heat transfer and its coupling with two-phase flow have received much attention and research efforts.[18–27] In the non-isothermal environment of fuel cells, the water vapor phase diffusion driven by temperature gradient can be important.[23,25] A dimensionless group Da was defined in our recent paper to characterize the two-phase flow regime inside a PEM fuel cell.[27]

Despite the great efforts in two-phase transport modeling of PEM fuel cells, little effort has been reported to compare liquid water prediction with experimental data, particularly in the through-plane direction. High-resolution neutron imaging[28–33] and X-ray[34,35] technique were developed in recent years and the experimental data of water through-plane profiles have been reported in the open literature. Weber and Hickner[36] and Wang and Chen[37] made the first attempts in comparing model predictions with the through-plane data from neutron imaging. However, model predictions from these authors failed to capture either the water content level[33,36] or local features such as liquid water trap[37] as detected by neutron imaging. Features of local maximum or minimum were also observed using the X-ray imaging technique.[35]

Following our previous effort in validating the through-plane water profile,[37] the present work explores one possible cause, namely the spatially-varying GDL properties, that is responsible for the local phenomena as observed by neutron imaging. Specifically, an attempt was made to model the effect of varying GDL properties and compare model prediction with experimental data. In practice, bipolar plates are usually placed over GDLs, which result in mechanical compression and deformation of GDLs, and the reduction of GDL thickness for the portion under lands. Consequently, land compression can lead to GDL property variation, and this effect on liquid water profiles is also investigated in the present work. Both 1-D and 2-D numerical studies were performed and computed results were compared with X-ray and neutron imaging data.

Mathematical Model

Governing equations.— Two-phase transport is modeled in the regions of the catalyst layers (CL), membrane, and GDLs, in conjunction with detailed electrochemical reaction kinetics in the catalyst layers. The model also accounts for the heat and electron transport in the bipolar plates, and consists of the conservation equations of mass, momentum, species, charges, and energy as follow:

$$\text{Continuity equation}: \quad \nabla \cdot (\rho \vec{u}) = 0 \qquad [1]$$

$$\text{Momentum conservation}: \quad \frac{1}{\varepsilon^2}\nabla \cdot (\rho \vec{u}\vec{u}) = -\nabla P + \nabla \cdot \rho\tau + S_u \qquad [2]$$

$$\text{Energy conservation}: \quad \nabla \cdot (\gamma_T \rho c_p \vec{u} T) = \nabla \cdot (k^{eff} \nabla T) + S_T \qquad [3]$$

$$\text{Reactant species conservation}: \quad \nabla \cdot (\gamma_k \vec{u} C_k) = -\nabla \cdot \vec{G}_{k,diff} + S_k \qquad [4]$$

$$\text{Water conservation}: \quad \nabla \cdot (\gamma_w \vec{u} C_w) = -\nabla \cdot (\vec{G}_{w,diff} + \vec{G}_{w,perm}) - \nabla \cdot \left[\left(\frac{m f_l^k}{M^k} - \frac{C_g^k}{\rho_g}\right)\vec{j}_l\right] + S_w \qquad [5]$$

* Electrochemical Society Active Member.
z E-mail: yunw@uci.edu

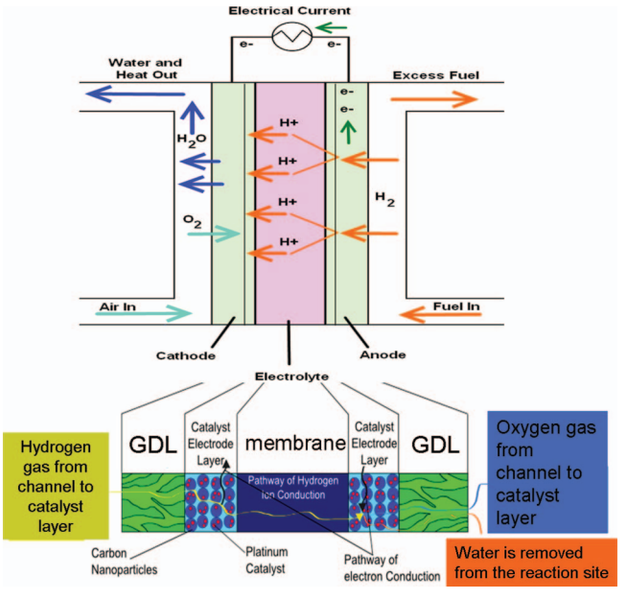

Figure 1. The schematic of a PEFC.[46]

$$\text{Charge conservation (protons)}: \quad 0 = \nabla \cdot \left(\sigma_m^{eff} \nabla \Phi^{(m)}\right) + S_{\Phi^{(m)}} \qquad [6]$$

$$\text{Charge conservation (electrons)}: \quad 0 = \nabla \cdot \left(\sigma_s^{eff} \nabla \Phi^{(s)}\right) + S_{\Phi^{(s)}} \qquad [7]$$

where ρ is the multiphase mixture density, $\vec{u}$ the superficial fluid velocity vector, p the pressure, C_k/C_w the molar concentration of reactant/water, T the temperature, $\Phi^{(m)}/\Phi^{(s)}$the electronic/electrolyte phase potentials. $\vec{G}_{diff}$ includes the diffusion fluxes in gaseous, liquid and solid electrolyte phases. $\vec{G}_{w,perm}$ represents the hydraulic permeation water flux through the membrane. Table I details the mathematic expressions of the sources terms. For a more complete model description, the readers can refer to our previous work.[37] The key aspects regarding the model and electrochemical/transport phenomena closely related to the topic of this paper are elaborated below.

Electrochemical kinetics.— During operation, fuel (usually hydrogen) and oxidant oxygen in ambient air are fed into the anode and cathode flow channels, respectively. They are reacted electrochemically within the catalyst layers with water and waste heat as the byproducts. In the anode, the hydrogen oxidation reaction (HOR) occurs: $H_2 \rightarrow 2H^+ + 2e^-$, while the oxygen reduction reaction (ORR) takes place in the cathode: $O_2 + 4e^- + 4H^+ \rightarrow 2H_2O$. The Butler-Volmer equation is customarily adopted to describe the electrochemical reaction rate. In PEFCs, the HOR is fast, thus yielding relatively small anode overpotential. Therefore, the anode reaction kinetics can be adequately simplified to a linear kinetic equation. For the ORR, sluggish kinetics results in large cathode overpotential. Consequently, the Butler-Volmer equation can be approximated by the Tafel kinetics. In addition, the reaction rate of the ORR highly depends on temperature as described by the Arrehenius expression. The HOR and ORR kinetic rate expressions are thus approximated by:

$$\text{HOR}: \quad j_a = \text{a} i_{0,a}^{ref} \left(\frac{C_{H2}}{C_{H2}^{ref}}\right)^{1/2} \left(\frac{\alpha_a + \alpha_c}{RT} \cdot F \cdot \eta\right) \qquad [8]$$

$$\text{ORR}: \quad j_c = -\text{a} i_{0,c}^{ref} \exp\left[-\frac{E_a}{R}\left(\frac{1}{T} - \frac{1}{353.15}\right)\right] \times \left(\frac{C_{O2}}{C_{O2}^{ref}}\right) \exp\left(-\frac{\alpha_c F}{RT} \cdot \eta\right) \qquad [9]$$

where E_a denotes the activation energy for ORR at the Pt/Nafion electrode and the surface overpotential is defined as:

$$\eta = \Phi^{(s)} - \Phi^{(m)} - U_o \qquad [10]$$

Two-phase transport in porous media.— Two-phase transport originates from the ORR's water production. In a PEFC, both the GDL and catalyst layer are highly porous media, where liquid may emerge in open pores when the water vapor partial pressure reaches the saturation pressure. Precisely dealing with two-phase flow is challenging, therefore various averaging methods have been proposed to simplify the model description without going into much microscopic details. In porous media, due to the random nature of the materials, the internal two-phase flows are more complicated, and usually their formulation follows the Darcy's law to relate the flux to pressure gradient. The mixture approach further simplifies the two-phase description by treating the multiple phases as a mixture with defined mixture properties. It has been successfully implemented in fuel cell modeling by various groups. In this approach, the two-phase mixture density is defined as:

$$\rho = s\rho^{(l)} + (1-s)\rho^{(g)} \qquad [11]$$

The saturation s can be obtained from the mixture water concentration C_w as follows:

$$s = \begin{cases} 0 & C_w \le C_{sat} \\ \dfrac{C_w - C_{sat}}{\rho^{(l)}/M_w - C_{sat}} & C_w > C_{sat} \end{cases} \qquad [12]$$

In porous media, the presence of one phase reduces the available pore space for transport in the other phase. The relative permeabilities $k_r^{(l)}$ and $k_r^{(g)}$ can be defined to account for this phase interaction, usually formulated as a function of liquid saturation. One expression for the relative permeabilities frequently adopted is as follows:

$$k_r^{(l)} = s^3 \text{ and } k_r^{(g)} = (1-s)^3 \qquad [13]$$

Water vapor transport.— In GDLs, diffusion is usually the dominant mechanism for vapor-phase transport. Convection can be a major force in some flow fields. Modeling vapor and gaseous reactants diffusion and convection has been attempted by many studies, therefore the detail is not repeated here. In the following we only explain the aspects closely related to two-phase flows. To account for liquid presence, we modify the effective diffusivity by:

$$D^{(g),eff} = [\varepsilon(1-s)]^{\tau_d} D^{(g)} \qquad [14]$$

The convection corrector factor γ is a function of s:

$$\gamma_w = \frac{\rho}{C_w}\left(\frac{\lambda^{(l)}}{M_w} + \frac{\lambda^{(g)}}{\rho^{(g)}} C_{sat}\right) \qquad [15]$$

Table I. Source terms of the conservation equations.[17]

	S_u	S_{C_k}	S_{C_w}	$S_{\Phi^{(m)}}$ / $S_{\Phi^{(s)}}$
Bipolar plates	–	–/–	–/–	–/0
Gas channels	$-\nabla P$	0	0	–
GDL	$-\frac{\mu}{K_{GDL}}\vec{u}$	0	0	–/0
Anode catalyst layer	$-\frac{\mu}{K_{CL}}\vec{u}$	$-\frac{j}{2F}$	0	j/–j
Cathode catalyst layer	$-\frac{\mu}{K_{CL}}\vec{u}$	$\frac{j}{4F}$	$-\frac{j}{2F}$	j/–j
Membrane	–	0	0	0/–

where $\lambda^{(l/g)}$are the relative mobilities of individual phases. The capillary pressure P_c, a primary driving force for liquid water transport, is given as follows:

$$P^{(g)} - P^{(l)} = P_c = \sigma \cos(\theta_c) \left(\frac{\varepsilon}{K}\right)^{1/2} J(s) \quad [16]$$

where σ is the surface tension. $J(s)$ for the hydrophobic diffusion media is given by:

$$J(s) = 1.417s - 2.120s^2 + 1.263s^3 \quad [17]$$

Once the capillary pressure is calculated, the flux $\vec{j}^{(l)}$ in the water equation of Eq. 5 can be obtained using the following equation:

$$\vec{j}^{(l)} = \frac{\lambda^{(l)}\lambda^{(g)}}{\nu} K[\nabla P_c + (\rho^{(l)} - \rho^{(g)})\vec{g}] \quad [18]$$

Water transport in the MEA.— Water in the Nafion membrane is bonded with the sulfonic acid groups in the ionomer. The water content λ is typically adopted to characterize the membrane hydration level and defined as the number of water molecules per sulfonic group. It is related to the equivalent water concentration through the following Eq.:[37]

$$C_w^m = \alpha \frac{\rho^{(m)}\lambda}{EW} \quad [19]$$

where $\rho^{(m)}$ and EW are the density and equivalent molecular weight of the membrane, respectively. Two processes shape the membrane water profile, one is the water electro-osmotic drag; the other is back transport including diffusion and hydraulic permeation. Detail of their mathematical description can be found in our previous work.[37]

Spatially-varying GDL property and its modeling.— In most of previous modeling studies, GDLs are treated as uniform media with constant properties in all the dimensions. With this treatment, the properties such as permeability and contact angle can be assumed constant and be taken out of in any spatial derivative operators in the governing equations. One example is to rearrange the expression of the capillary action as a "diffusive" term, using the following 1-D problem as an example:

$$\frac{\lambda^{(l)}\lambda^{(g)}}{\nu} K \frac{dP_c}{dx} = -D_c \frac{ds}{dx} \quad [20]$$

where $D_c = -\frac{\sigma}{\nu}\cos(\theta_c)(K\varepsilon)^{1/2} k_{rl} \frac{dJ(s)}{ds}$. In the absence of any sources of water within a GDL, there exists no local maximum or minimum inside the GDL at steady state. Figure 2 presents the 1-D isothermal model predictions based on Eq. 20 at various conditions. It can be seen that the water saturation deceases monotonically from the left to right or from the catalyst layer side to the channel. Similar profiles have been reported by Pasaogullari and Wang,[13] and Wang and Chen.[37] However, the above analysis is only valid under the assumption of uniform GDL properties. When a spatial property variation is present, the above transform becomes invalid. In this case, extra terms must be added to account for this spatial variation based on the product rule of derivatives. For example, upon a spatial variation of permeability the following term should be added to the right side of Eq. 20:

$$\frac{\lambda_l \lambda_g \sigma \cos(\theta_c)\varepsilon^{1/2}}{\nu} J(s) K \frac{d}{dx}(K^{-1/2}) \quad [21]$$

This term can raise local maximum/minimums in the water profiles. It is also physically sound: for example, the media with larger pores can trap more water. Such maximums and minimums were observed in both X-ray imaging[35] and high-resolution neutron imaging

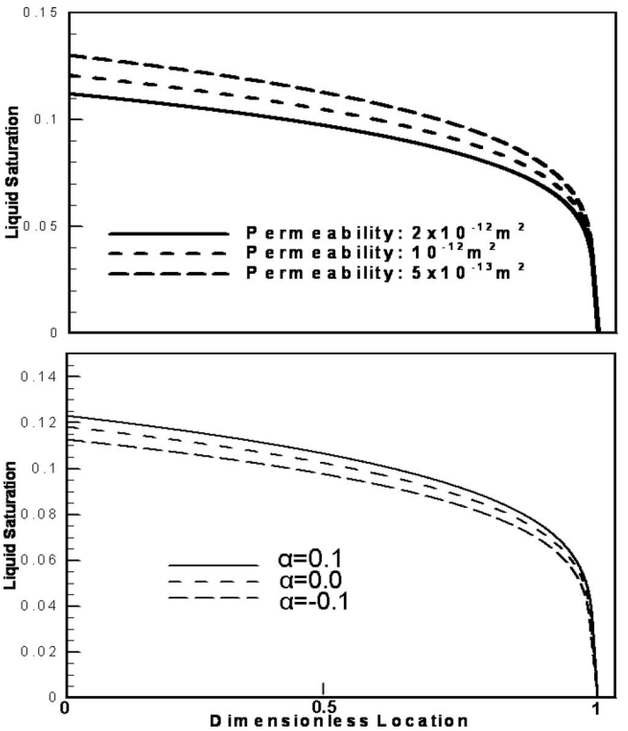

Figure 2. 1-D model prediction of liquid water profile across a cathode GDL using a uniform property across the GDL: (a) different permeabilities; (b) different net water transfer coefficients.

experiments.[29,32] However, few studies were reported in which the effect of spatial variation of GDL properties was investigated. Recently, Hinebaugh *et al*.[38] experimentally measured the local porosity of a carbon paper, showing a spatially-varying porosity of GDLs as presented in Fig. 3. The variation may be caused by the material fabrication process. Carbon papers are a typical GDL material based on carbon fibers. It is non-woven and the fibers are tied by binders as shown in Fig. 4 ,[26] and the fiber dimension is around 10 μm in its crosssection. Though the fibers are placed randomly and the binders appear also randomly,[39,40] local heterogeneity may occur. In a fabricated carbon paper, the average pore size is around 10-30 μm with large pores can reach ∼50 μm.[41,42] As a result of porosity variation, the permeabil-

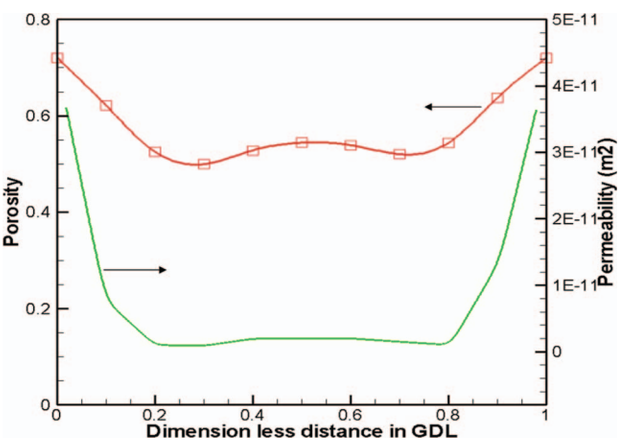

Figure 3. The spatial variation of porosity[38] and corresponding permeability across a GDL calculated by the Blake-Kozeny equation.

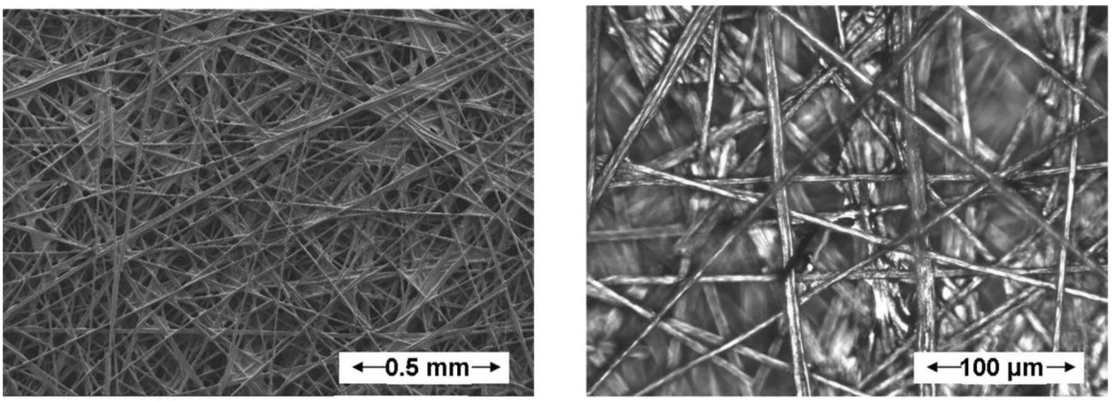

Figure 4. Microscopy images of a carbon paper.[40]

ity, a factor that has a great impact on two-phase flow, also varies spatially, as indicated by the following Blake-Kozeny equation:

$$K = \frac{D_p^2}{150}\frac{\varepsilon^3}{(1-\varepsilon)^2} \quad [22]$$

where D_p is the pore dimension. The calculated permeability profile is plotted in Fig. 3 as well, by considering a uniform compression ratio of 0.72. By applying the permeability profile in both anode and cathode GDLs, we obtained the liquid water distribution that is very close to the one probed by X-ray imaging as displayed in Fig. 5.

In addition to porosity and permeability, the spatial changes in other properties may have similar impacts. For example, given that the capillary pressure P_c is also a function of contact angle and surface tension, i.e.,$P_c(\sigma, \theta_c, \varepsilon, K, s)$, changes in contact angle and surface tension will lead to similar effects. A more general expression of the water flux driven by the capillary pressure gradient accounting for spatially-varying GDL properties can be derived as follow:[43]

$$\frac{\lambda_l\lambda_g}{\nu}K\nabla P_c(\sigma,\theta_c,\varepsilon,K,s) = \frac{\lambda_l\lambda_g}{\nu}K\left(\frac{\partial P_c}{\partial\sigma}\nabla\sigma + \frac{\partial P_c}{\partial\theta_c}\nabla\theta_c + \frac{\partial P_c}{\partial\varepsilon}\nabla\varepsilon + \frac{\partial P_c}{\partial K}\nabla K + \frac{\partial P_c}{\partial s}\nabla s\right) \quad [23]$$

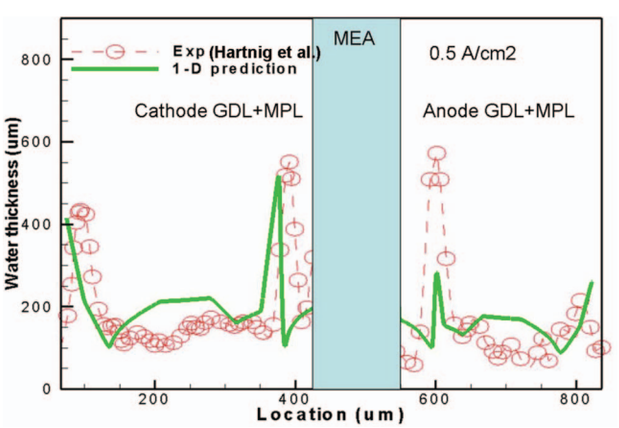

Figure 5. 1-D prediction of liquid water profile across the anode and cathode GDLs, and comparison with the X-ray imaging data.[35]

Boundary conditions.— Equations 1–17 form a complete set of governing equations with ten unknowns: $\vec{u}$ (with three components), P, C_k (O_2 and H_2), C_w, T, $\Phi^{(m)}$, and $\Phi^{(s)}$. Their corresponding boundary conditions are presented in detail in our previous work[37] and thus are not repeated here.

Numerical Procedures

The governing equations, Eqs. 1–17, along with the associated boundary conditions are discretized by the finite volume method and solved in the commercial CFD software package, Fluent® (version 6.0.12), by the SIMPLE (semi-implicit pressure linked equation) algorithm. The SIMPLE algorithm updates the pressure and velocity fields from the solution of a pressure correction equation, solved by the algebraic multi-grid (AMG) method. Following the solution of the flow field, the energy, species, proton, and electron equations are solved. The source terms and physical properties are implemented in a UDF (user-defined function) and the species/charge transport equations are solved through the software's user-defined scalars. Though the focus is placed on one dimension, i.e. the through-plane direction, it is important to conduct a multi-dimensional study because the through-plane data from neutron imaging are usually obtained through averaging over the other two dimensions. In particular, the channel-land structure should be captured in the numerical study in order to account for the increased transport resistance for the region under the

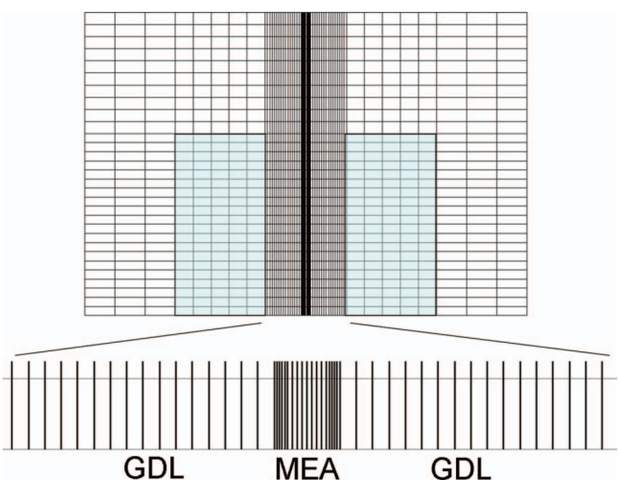

Figure 6. The 2-D computational domain of the fuel cell.

Table II. Geometrical, physical and operating parameters.

Quantity	Value
Channel depth/width and land width	1.0/1.5 and 1.0 mm
Catalyst layer/Membrane thickness	0.01/0.03 mm
Anode/cathode GDL thickness	0.2 mm
Anode/cathode pressures, P	2.0/2.0 atm
Porosity of GDLs/catalyst layers, ε	0.6/0.5
Humidification in the anode and cathode	100/100%
Water concentration correction factor, α	0.15
Volume fraction of ionomer in catalyst layers, ε_m	0.2
Electronic conductivity of GDLs/bipolar plates, σ_s^{eff}	500/2000 W m^{-1} K^{-1}
Viscosity of liquid water, μ_l	3.5×10^{-4}kg/m s
Permeability of membrane, K_m	$5 \times 10^{-20}m^2$
Surface tension, liquid-water-air (80°), τ	0.0625 N/m
Thermal conductivity of the membrane/catalyst layer/GDL/bipolar plate	0.95/3.0/5.0/20.0 W/m K
Contact angle of the GDL, θ_c	120°
Exchange current density × reaction surface area, $a_0 i_{0,a}/a_0 i_{0,c}$	$1.0\times10^9/0.5\times10^4$ A m^{-3}

land. The computational mesh of the PEFC employed for the 2-D numerical study is shown in Fig. 6. Totally, about 50 gridpoints are adopted in the through-plane direction for the GDLs (both anode and cathode) to precisely capture the liquid transport. 30 gridpoints are employed in the in-plane direction to capture the land-channel feature, where 10 points are placed for the land and 20 for the channel. The geometrical and operating parameters are listed in Table II. In all the simulations to be presented in the next section, the converged values of species imbalance (i.e. H_2, O_2 and H_2O) are all less than 1% and absolute equation residuals are smaller than 10^{-6}.

Results and Discussion

The first case of numerical study in the present work is based on the fuel cell geometry employed in our previous validation effort.[37] The computational domain is the same as that used previously. The model prediction based on a uniform GDL property is plotted in Fig. 7a using the solid line, in comparison with the neutron imaging data. It can be seen that though the model prediction with a uniform GDL property agrees reasonably well with the neutron imaging data, the local maximum and minimum within the cathode GDL shown by the neutron imaging are not captured by the model prediction. We also applied the Gaussian smoothing technique, outlined in Ref. 37, to account for the geometric blur or other uncertainties arising from the neutron imaging, and the smoothed curve is also plotted in the figure. However, smoothing only blurs (or change) the sharp corner, thus is not expected to alter the model prediction to simulate the observed local maximums or minimums. To explore these local distinctions observed in the previous work, we include a non-uniform GDL property just near the location of the local cathode maximum in the neutron imaging curve, see Fig. 7b. The predicted curve is also plotted in the figure (see the dashed green curve in Fig. 7a). It can be seen that the local features are well captured by the model prediction when spatially-varying GDL property is employed. Note that in this case study we only consider the permeability variation results from the changing porosity, following the previous case (see Fig. 3). As indicated by Eq. 23, other properties such as contact angle can also cause similar effect.

It is worthy to note that the through-plane water profiles obtained from neutron imaging are usually averaged over the other two dimensions, i.e. the in-plane and along-channel directions. In reality, the basic land-channel structure of a PEM fuel cell can lead to liquid water saturation variation in the in-plane direction because of the increased transport resistance under the lands. Tabuchi et al.[44] revealed that

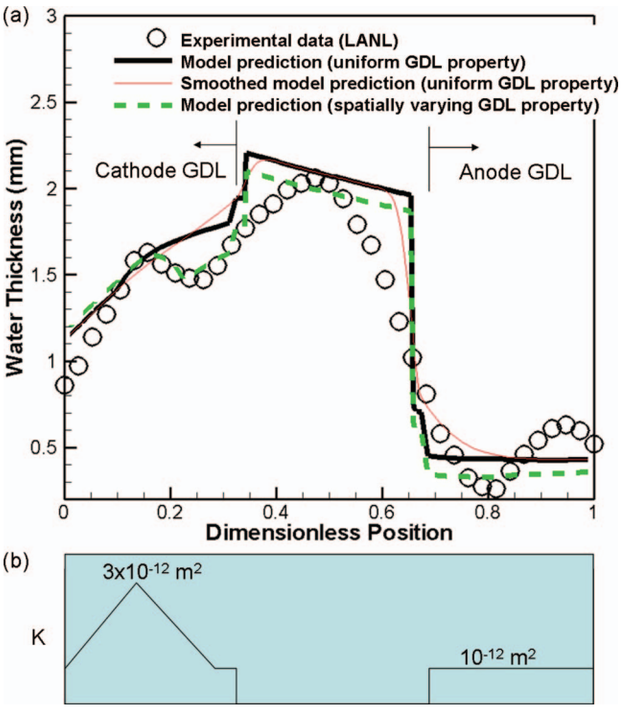

Figure 7. (a): Comparison with the high resolution neutron imaging data, 2-D model prediction (with/without smoothing) using a uniform GDL property, and 2-D model prediction using a spatially-varying GDL property;[37] (b) The varying GDL property in the present study.

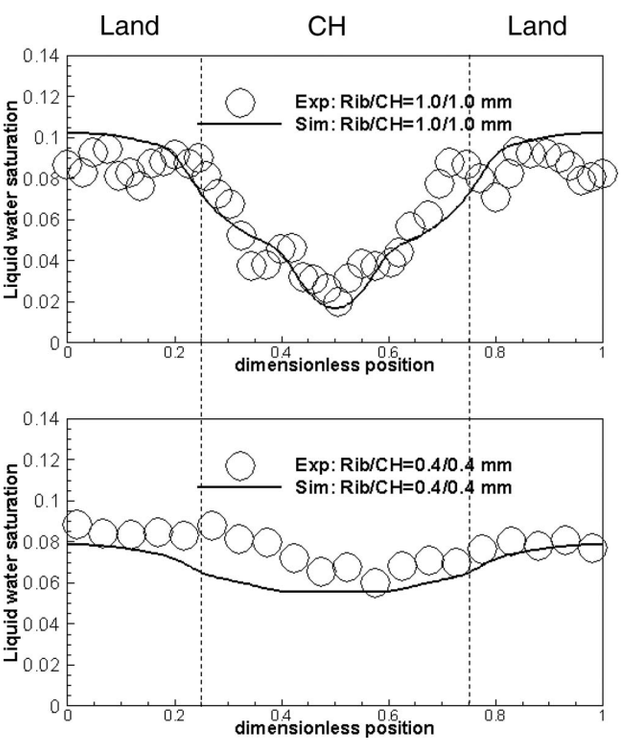

Figure 8. Comparison with the in-plane liquid water profiles obtained by neutron imaging from Tabuchi et al.[44] The GDL material property in the present study is chosen close to that suggested by Tabuchi et al., e.g. the GDL porosity is 0.6, tortuosity 2.75, contact angle 120°, and thermal conductivity 2.5 W/m K. The cell is operated at 2.5 A/cm^2 and 80°C.

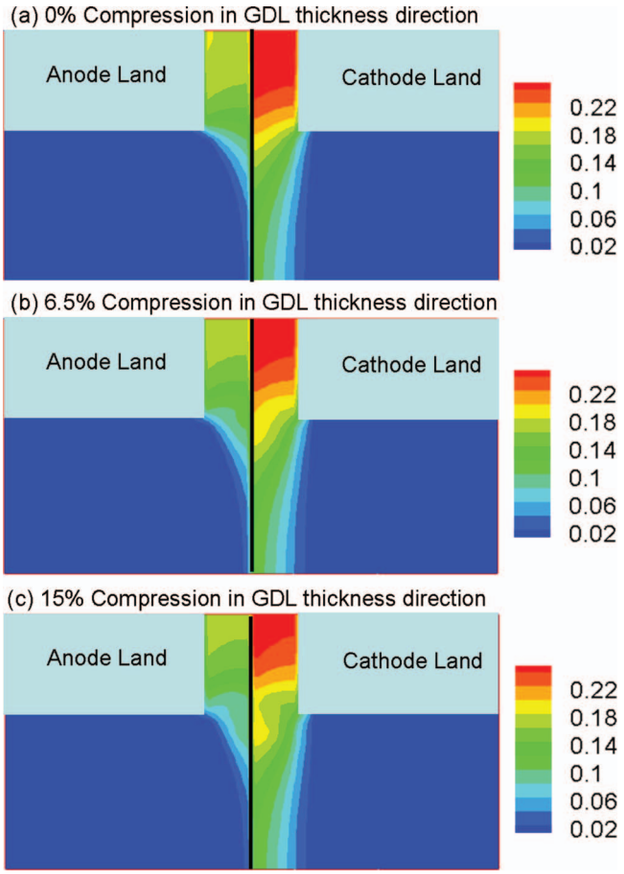

Figure 9. Liquid water saturation contours at different GDL compression ratios under the operating condition of 0.8 A/cm^2, 80 °C, and 2 atm.

liquid saturation is higher under the lands using neutron imaging. Therefore, the in-plane water profile must be precisely captured in order to validate the through-plane neutron imaging data. Fig. 8 compares our 2-D model prediction with the neutron imaging data from Tabuchi et al.[44] The GDL material properties in the model are also chosen according to the ones used in Tabuchi et al. It can be seen that the in-plane liquid water profiles are reasonably captured by our 2-D model.

In addition to the structural heterogeneity arising from GDL fabrication, another cause of spatially-varying property may result from fuel cell assembly, i.e. land compression. Upon compression, the GDL thickness under the lands is reduced and hence the porosity. The degree of compression or compression ratio (CR) can be defined by the ratio of the compressed GDL thickness to the uncompressed one. The resultant porosity can be evaluated by the following formula:

$$\varepsilon = \frac{\varepsilon_0 - CR}{1 - CR} \qquad [24]$$

where ε_0 is the uncompressed GDL porosity. As shown in Eq. 22, the local permeability will be reduced as well after compression. Fig. 9 shows the liquid saturation contours, computed by the present model, for two different compression scenarios in comparison with the non-compression case. It can be seen that with compression the liquid water saturation under the land decreases. For the compression (CR) of 15%, i.e. the thickness of the GDL is reduced by 15%, on the cathode side there appears a minimum in the liquid saturation near the interface between the land and channel. This can be explained by the more compact GDL under the land, which contains lower liquid saturation in the pore to balance the liquid capillary pressure in the vicinity of the uncompressed portion of the GDL, i.e. under

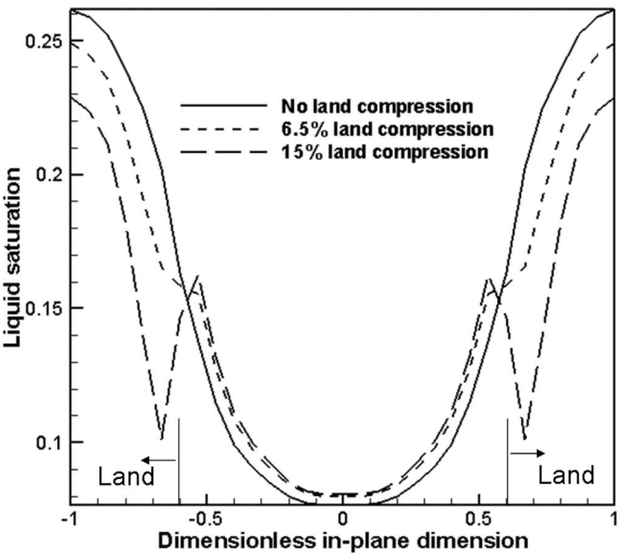

Figure 10. Liquid water saturation profiles in the in-plane direction at different GDL compression ratios under the operating condition of 0.8 A/cm^2, 80 °C, and 2 atm.

the channel. Figure 10 plots the liquid water saturation profiles in the in-plane direction for the three cases. The saturation is averaged over the other two dimensions. It can be seen that the land compression can greatly affect the liquid water profile under the land, particularly near the land-channel edge. At the CR of 15%, there appears a significant discontinuity near the edge.

Figure 11 displays the comparison of model prediction and neutron imaging data of liquid water profiles for both under the channel and land. It can be seen that in the middle of the GDL, there appears

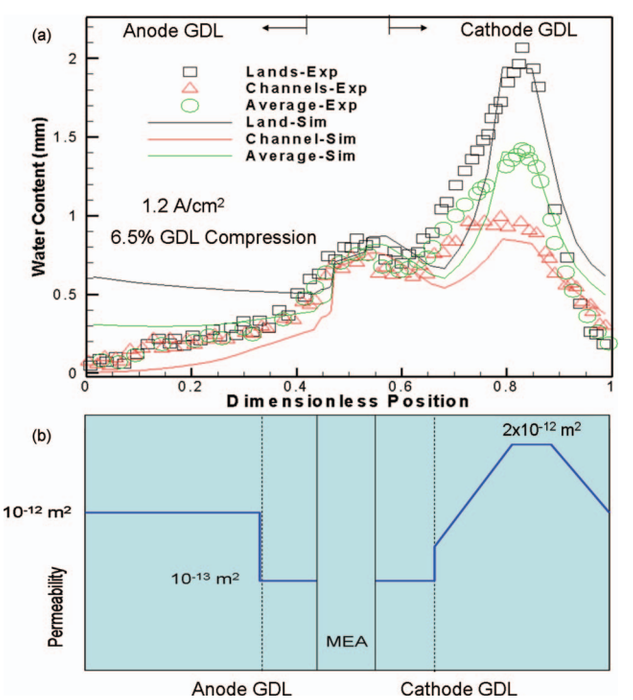

Figure 11. Comparison of the 2-D model prediction and neutron imaging data (from LANL[45]) (a); and the spatially-varying property of the GDL in the simulation (b).

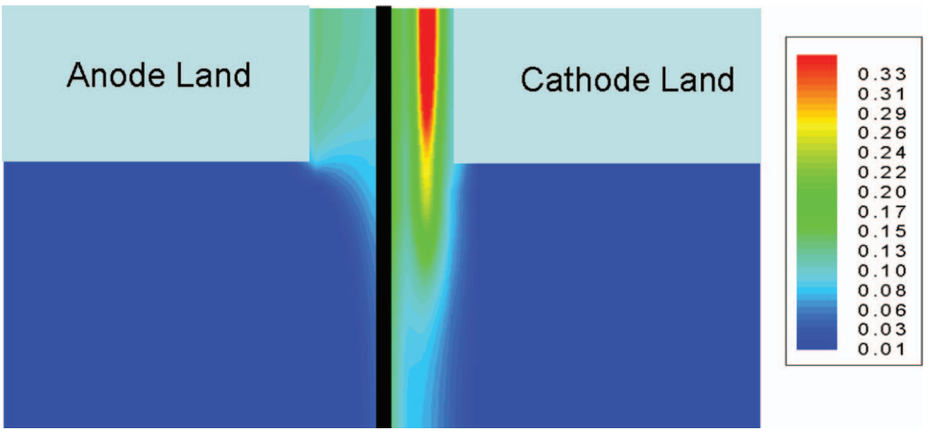

Figure 12. Predicted 2-D contours of the liquid water saturation.

maximum water contents at both locations in the neutron imaging data. In the simulation, we chose a 6.5% land-compression and varying GDL property in the through-plane direction as shown in Figure 11b in order to achieve the best match with the experimental data. The location of the maximum water content has the local large permeability because larger permeability traps more water locally. In addition, the under-land area shows a much higher water content comparing with the under-channel region in the cathode, which is due to the high liquid water resistance for the under-land region. Note that in the anode we consider a uniform property in the GDL and in the MPL (microporous layer), respectively, therefore the predicted curve does not agree with the neutron imaging data very well. We didn't consider a varying GDL property in the anode, because our focus is to elucidate how the GDL spatial varying property alters the water profile. We use the cathode side as an example, where the liquid effect may be more important. For a full validation of both anode and cathode sides, we think it is more proper to incorporate the experimentally determined GDL property variation in both anode and cathode. We shall consider doing this in our future work.

Figure 12 presents the liquid water saturation contours. It can be seen that there exists a large amount of liquid accumulated in the location where the local permeability is high under the cathode land. The liquid saturation can reach as high as 35%. Under the cathode channel, the local maximum is not as remarkable as that under the land. On the anode side, part of the region under the channel is free of liquid water, which is due to the local heating by fuel cells.[37] This also explains the low water content in the anode that is observed in the in-situ neutron imaging, see Fig. 11.

The local liquid water trapped inside the GDL can have a significant effect on fuel cell performance. This is because the liquid occupies part of the pore space that is for gas reactant supply. The predicted cell voltage with non-uniform GDL properties is 0.55 V whereas that using uniform GDL properties gives 0.58 V. Further study is needed to compare with the experimental measurement in terms of both neutron imaging data and cell voltage by incorporating experimentally determined GDL properties. In addition, the local bulk water makes GDL dewetting to occur more slowly (that is, it takes a longer duration to dewet by evaporation). Residual liquid can raise GDL degradation during subfreezing season due to ice formation.

Conclusions

A non-isothermal two-phase model of PEM fuel cells was developed, which accounts for the effects of spatial variation of GDL property and land compression. 1-D and 2-D numerical simulations were carried out to investigate these effects on liquid water through-plane profiles. It was found that the varying GDL property can give rise to local maximum or minimum in liquid water profiles, in sharp contrast with the scenario of a uniform GDL property which yields monotonical change in isothermal liquid profile across the GDL. Based on an experimentally determined GDL property, 1-D model prediction was first computed and the result agrees reasonably well with the liquid water curve obtained by the X-ray imaging technique. 2-D model prediction was further computed and compared with previous results obtained using uniform GDL property, and also with the neutron imaging data. The numerical results indicate that the new model prediction using spatial variation of GDL property reasonably captures the local maximum or minimum in GDLs as observed by neutron imaging. In addition, the effect of land compression was modeled by incorporating the GDL property change upon compression. Numerical results indicate that land compression can lower the liquid saturation under the land and give rise to a substantial impact with 15% compression. Model validation of liquid water profiles under land and channels, respectively, were also performed and the computed model predictions agree reasonably well with the neutron imaging data.

Acknowledgments

Funding support of this work was provided by Sandia National Laboratories. Sandia is a multiprogram laboratory operated by Sandia Corporation, a Lockheed Martin Company for the United States Department of Energy's National Nuclear Security Administration under contract DE-AC04-94AL85000. Partial support of this work by the Academic Senate Council on Research, Computing & Library Resources at UCI is also gratefully acknowledged.

Appendix: Nomenclature

C	molar concentration, mol/m^3
D	mass diffusivity of species, m^2/s
F	Faraday's constant, 96,487 C/equivalent
$\vec{G}$	species diffusion/permeation flux, mol m^{-2}
I	current density, A/ cm^2
$\vec{i}$	superficial current density, A cm^{-2}
j	transfer current density, A cm^{-3}
$\vec{j}^{(l)}$	mass flux of liquid phase, kg m^{-2} s^{-1}
K	permeability, m^2
k_r	relative permeability
M	molecular weight, kg/mol
P	pressure, Pa
R	gas constant, 8.134 J/mol K
s	liquid saturation
S	source term in transport equations
T	temperature, K
U_o	equilibrium potential, V
$\vec{u}$	velocity vector, m/s

Greek

α	Water concentration correction factor
ε	porosity
Φ	phase potential, V
$\vec{\vec{\tau}}$	shear stress, N m^{-2}
λ	membrane water content
$\lambda^{(k)}$	mobility of phase k
υ	kinematic viscosity, m^2/s
σ	surface tension, N/m
ρ	density, kg/m^3
γ_c	correction factor for species convection
η	surface overpotential, V

Superscripts and Subscripts

a	anode
c	cathode
d	electro osmotic drag
eff	effective value
GDL	gas diffusion layer
g	gas phase
k	species; liquid or gas phase
l	liquid
m	membrane
o	reference value
perm	permeation
s	liquid saturation or solid phase

References

1. Y. Wang, K. S. Chen, J. Mishler, S. C. Cho, and X. C. Adroher, *Applied Energy*, **88** (2011) 981–1007.
2. C. Y. Wang, *Chem. Rev.* (Washington, D.C.), **104**, 4727 (2004).
3. A. Z. Weber and J. Newman, *Chem. Rev.* (Washington, D.C.), **104**, 4679 (2004).
4. V. Gurau and J. A. Mann, *SIAM J Appl Math* **70** (2) (2009), pp. 410–454.
5. C. Siegel, *Energy* **33** (9) (2008), pp. 1331–1352.
6. N. Djilali, *Energy* **32** (4) (2007), pp. 269–280.
7. M. Bavarian, M. Soroush, I. G. Kevrekidis, and J. B. Benziger, *Industrial and Engineering Chemistry Research*, **49** (17), 7922–7950, 2010.
8. Z. H. Wang, C. Y. Wang, and K. S. Chen, *J. Power Sources*, **94**, 40 (2001).
9. W. He, J. S. Yi, and T. V. Nguyen, *AIChE J.*, **46**, 2053 (2000).
10. D. Natarajan and T. V. Nguyen, *J. Electrochem. Soc.*, **148**, A1324 (2001).
11. L. You and H. Liu, *Int. J. Heat Mass Transfer*, **45**, 2277 (2002).
12. A. Z. Weber, R. M. Darling, and J. Newman, *J. Electrochem. Soc.*, **151**, 1715 (2004).
13. U. Pasaogullari and C. Y. Wang, *J. Electrochem. Soc.*, **151**, 399 (2004).
14. U. Pasaogullari and C. Y. Wang, *Electrochim. Acta*, **49**, 4359 (2004).
15. C. Ziegler, H. M. Yu, and J. O. Schumacher, *J. Electrochem. Soc.*, **152**, A1555 (2005).
16. H. Sun, H. Liu, and L.-J. Guo, *J. Power Sources*, **143**, 125 (2005).
17. Y. Wang, *J. Power Sources*, **185**, 261 (2008).
18. J.-H. Nam and M. Kaviany, *Int. J. Heat Mass Transfer*, **46**, 4595 (2003).
19. J. Yuan and B. Sunden, *Electrochim. Acta*, **50**, 677 (2004).
20. T. Berning and N. Djlali, *J. Electrochem. Soc.*, **150**, A1589 (2003).
21. S. Mazumder and J. V. Cole, *J. Electrochem. Soc.*, **150**, 1510 (2003).
22. E. Birgersson, M. Noponen, and M. Vynnycky, *J. Electrochem. Soc.*, **152**, A1021 (2005).
23. Y. Wang and C. Y. Wang, *J. Electrochem. Soc.*, **153**, A1193 (2006).
24. A. Z. Weber and J. Newman, *J. Electrochem. Soc.*, **153**, A2205 (2006).
25. Y. Wang and C. Y. Wang, "Two-Phase Transients of Polymer Electrolyte Fuel Cells," *J. Electrochem. Soc.*, **154** (2007) B636–643.
26. Y. Wang, C. Y. Wang, and K. S. Chen, *Electrochimica Acta*, **52**, 3965–3975 (2007).
27. Y. Wang and Ken S. Chen, "Elucidating two-phase transport in a polymer electrolyte fuel cell, Part 1: characterizing flow regimes with a dimensionless group", *Chemical Engineering Science*, in press.
28. J. P. Owejan, T. A. Trabold, and D. L. Jacobson, M. Arif, and S. G. Kandlikar, *Int. J. Hydrogen Energy*, **32**, 4489 (2007).
29. M. A. Hickner, N. P. Siegel, K. S. Chen, D. S. Hussey, D. L. Jacobson, and M. Arif, *J. Electrochem. Soc.*, **155**, B294 (2008).
30. D. S. Hussey, D. L. Jacobson, M. Arif, J. P. Owejan, J. J. Gagliardo, and T. A. Trabold, *J. Power Sources*, **172**, 225 (2007).
31. M. A. Hickner, N. P. Siegel, K. S. Chen, D. S. Hussey, D. L. Jacobson, and M. Arif, *J. Electrochem. Soc.*, **155**, B427 (2008).
32. R. Mukundan and R. L. Borup, *Fuel Cells*, **9**, 499 (2009).
33. R. Borup, Water Transport Exploratory Studies, DOE Hydrogen Program Review, May 18–22, 2009.
34. P. K. Sinha, P. Halleck, and C.-Y. Wang, *Electrochem. Solid-State Lett.*, **9**, A344 (2006).
35. C. Hartnig, I. Manke, R. Kuhn, N. Kardjilov, J. Banhart, and W. Lehnert, *Applied Physics Letters*, **92**, 134106, (2008).
36. A. Z. Weber and M. A. Hickner, *Electrochim. Acta*, **53**, 7668 (2008).
37. Y. Wang and K. S. Chen, *J. Electrochem. Soc.*, **157** (12) B1878–B1886 (2010).
38. J. Hinebaugh, Z. Fishman, and A. Bazylak, *Proceedings of the ASME 2010 Eighth International Fuel Cell Science, Engineering and Technology Conference*, FuelCell2010-33097, June 14–16, 2010, Brooklyn, New York, USA.
39. R. Thiedmann, F. Fleischer, Ch. Hartnig, W. Lehnert, and V. Schmidt, Stochastic 3D modeling of the GDL structure in PEM fuel cells based on thin section detections, *J. Electrochem. Soc.* **155** (2008) B391–B399.
40. Y. Wang, S. Cho, R. Thiedmann, V. Schmidt, W. Lehnert, and X. Feng, "Stochastic Modeling and Direct Simulation of the Diffusion Media for Polymer Electrolyte Fuel Cells", *International Journal of Heat and Mass Transfer*, **53**, 1128–1138 (2010).
41. M. Mathias, J. Roth, J. Fleming, and W. Lehnert, in: W. Vielstich, H. Gasteiger, A. Lamm (Eds.), *Handbook of Fuel Cells: Fundamentals, Technology and Applications*, vol. 3, John Wiley & Sons Ltd., 2003.
42. J. Benziger, J. Nehlsen, D. Blackwell, and T. Brennan, J. Itescu, *J. Mem. Sci.* **261** (2005) 98.
43. Y. Wang, Suman Basu, and Chao-Yang Wang "Modeling Two-Phase Flow in PEM Fuel Cell Channels", *Journal of Power Sources*, **179** (2008) 603–617.
44. Y. Tabuchi, T. Shiomi, O. Aoki, N. Kubo, and K. Shinohara, Effects of heat and water transport on the performance of polymer electrolyte membrane fuel cell under high current density operation, *Electrochimica Acta* **56** (2010) 352–360.
45. J. S. Spendelow, R. Mukundan, J. R. Davey, J. D. Fairweather, D. Spernjak, R. L. Borup, D. S. Hussey, D. L. Jacobson, *Effect of GDL on Water Distribution in Operating PEMFCs: High-Resolution Neutron Radiography, the 218th Electrochemical Society Meeting*, Las Vegas, Nevada, October 10–15, 2010.
46. M. Gundevia and Y. Wang, Private Communication.